ADVANCED FUNCTIONAL MATERIALS
www.afm-journal.de

Conjugated Porous Polymers Based on BODIPY and BOPHY Dyes in Hybrid Heterojunctions for Artificial Photosynthesis

Laura Collado, Teresa Naranjo, Miguel Gomez-Mendoza, Carmen G. López-Calixto, Freddy E. Oropeza, Marta Liras,* Javier Marugán,* and Víctor A. de la Peña O'Shea**

Developing highly efficient photocatalysts for artificial photosynthesis is one of the grand challenges in solar energy conversion. Among advanced photoactive materials, conjugated porous polymers (CPPs) possess a powerful combination of high surface areas, intrinsic porosity, cross-linked nature, and fully π-conjugated electronic systems. Here, based on these fascinating properties, organic–inorganic hybrid heterostructures composed of CPPs and TiO_2 for the photocatalytic CO_2 reduction and H_2 evolution from water are developed. The study is focused on CPPs based on the boron dipyrromethene (BODIPY) and boron pyrrol hydrazine (BOPHY) families of compounds. It is shown that hybrid photocatalysts are active for the conversion of CO_2 mainly into CH_4 and CO, with CH_4 production 4 times over the benchmark TiO_2. Hydrogen evolution from water surpassed by 37.9-times that of TiO_2, reaching 200 mmol g_{cat}^{-1} and photonic efficiency of 20.4% in the presence of Pt co-catalyst (1 wt% Pt). Advanced photophysical studies, based on time-resolved photoluminescence and transient absorption spectroscopy, reveal the creation of a type II heterojunction in the hybrids. The unique interfacial interaction between CPPs and TiO_2 results in longer carriers' lifetimes and a higher driving force for electron transfer, opening the door to a new generation of photocatalysts for artificial photosynthesis.

1. Introduction

In a world struggling to limit global warming to below 2 °C, finding alternative renewable energy resources has become imperative to fulfill the increasing energy demand and to reduce the current heavy reliance on fossil fuels. Solar energy is the largest exploitable renewable energy source, providing more energy to the Earth per hour than the total energy consumed by human activities in a year.[1] Moreover, it has the potential to be clean, cheap, renewable and sustainable, although it must be captured and transformed into useful forms of energy to address the intermittency of the day/night cycles and weather patterns.[2] Solar energy can be directly converted into renewable and carbon-neutral fuels, which are stable in storage, safe in transportation, and can release energy when needed.[3] This innovative approach, known as artificial photosynthesis (AP) when driven under mild conditions, has become a research hotspot for the development of alternative and economically competitive solar fuels.[4] Learning from the natural photosynthesis process, AP systems are able to efficiently capture and convert solar energy, and then store it in the form of chemical bonds.[2] Solar energy is therefore used to split water and produce hydrogen, and/or to transform carbon dioxide and water into a renewable source of energy-rich carbon-containing products, or even to fix N_2 into ammonia.[5] The major products of the photocatalytic CO_2 reduction include carbon monoxide (CO), methane (CH_4), methanol (CH_3OH), and C_{2+} hydrocarbons, such as ethylene (C_2H_4), ethane (C_2H_6), and ethanol (C_2H_5OH),[3] which in a future energy scenario could represent carbon-neutral fuels produced from renewable electricity, water, and the circular use of CO_2. Besides, solar fuels are more viable for massive energy storage than conventional electricity systems, since they are considered high-density fuels that could be used directly for transportation in tankers or gas pipes, as raw materials for industry, or for electricity production in fuel cells or turbines, thus representing a scalable pathway to transport renewable energy globally.[1,5,6]

Generally, AP photocatalysts must provide: 1) efficient light absorption; 2) long-lived charge separated states; and 3) minimal back-reaction rates and product crossover.[5,6] These requirements depend largely on the nature of the photocatalyst and the rational design of its components. Well-defined hybrid heterojunctions between inorganic semiconductors (IS) and

L. Collado, T. Naranjo, M. Gomez-Mendoza, C. G. López-Calixto, F. E. Oropeza, M. Liras, V. A. de la Peña O'Shea
Photoactivated Processes Unit
IMDEA Energy Institute
Parque Tecnológico de Móstoles
Avda. Ramón de la Sagra 3, Madrid, Móstoles 28935, Spain
E-mail: laura.collado@urjc.es; marta.liras@imdea.org; victor.delapenya@imdea.org
L. Collado, J. Marugán
Department of Chemical and Environmental Technology
ESCET
Universidad Rey Juan Carlos
C/ Tulipán s/n, Madrid, Móstoles 28933, Spain
E-mail: javier.marugan@urjc.es
The ORCID identification number(s) for the author(s) of this article can be found under https://doi.org/10.1002/adfm.202105384.

DOI: 10.1002/adfm.202105384

organic polymers (OP) are gaining attention, mainly due to their extended light absorption range and better quantum efficiencies compared to conventional catalysts.[7–9] Conjugated porous polymers (CPPs), a class of π-conjugated organic polymers, have recently emerged as an interesting counterpart due to the possibility of controlling their optoelectronic, textural and morphological properties at the molecular level.[10–12] The tunable nature of these polymers in turn confers desirable properties for photocatalysts, such as adjustable bandgaps, high surface areas, micro- or mesoporosity, thermal stability, and high flexibility.[13,14]

In the hybrid heterojunction, the CPP acts as an organic semiconductor that generally possesses a less energetic bandgap than that of the inorganic semiconductor counterpart. Besides, its highest occupied molecular orbital (HOMO) and lowest occupied molecular orbital (LUMO) energy levels are located at higher energetic positions than the conduction and valence bands of the inorganic semiconductor.[15] The charge transfer mechanism between both organic and inorganic semiconductors can occur through three different pathways: i) sensitization; ii) type II heterojunction; or iii) Z-scheme mechanism.[7] The synergy between CPPs and ISs consequently results in an extended light absorption range, improved textural properties and higher stability to photocorrosion. Interestingly, these hybrid heterostructures can effectively facilitate the charge transfer and reduce the recombination of photogenerated electrons and holes, resulting in enhanced photocatalytic performances.[13,16] Due to their remarkable advantages, CPPs have recently attracted significant attention as promising photocatalysts for solar fuel generation, particularly for hydrogen evolution.[7,10,11,13,14]

In order to explore advanced materials with potential application in AP, here we investigate the use of conjugated porous polymers as part of hybrid materials for CO_2 photoreduction and H_2 evolution from water. Among the possible moieties to synthesize CPPs, boron-centered fluorophores have been selected because of their excellent photophysical properties and high photostability. Some of the more successful fluorophores in the literature belong to the boron dipyrromethene (BODIPY; see **Figure 1** left) family of compounds. These dyes, which are composed of a dipyrromethene bound to a central BF_2 unit, present an excellent chemical versatility for their use in a myriad of (bio)technological fields, from (bio)medicine[17–19] to energy conversion in photovoltaic devices,[20] solid state lasers[21] or hydrogen production.[22–24] BODIPY-based CPPs have been also used as heterogeneous photocatalysts in organic transformations,[25,26] gases adsorption,[27] sensing,[28,29] and electrode materials,[30] among others. In addition, an analog to BODIPY dyes has emerged in the last few years, known as BOPHYs (boron pyrrol hydrazine, see Figure 1 right). Although these new dyes are structurally close to BODIPYs, they have two chelating positions amenable for linking boron. In both dyes, the synthetic access involves boron chelation of a π-conjugated pyrrole-based system, but, in the BOPHY case, it includes a central hydrazine-based spacer.[31,32] BOPHY dyes have been proven to be excellent photoactive materials suitable for several applications. In fact, we have reported the synthesis of BOPHY-based CPPs as photocatalysts for oxidation of organic sulfides,[33] hydrogen production,[34] and also as part of a photon upconversion system.[35]

Despite the versatility of conjugated polymers, their limited use in CO_2 photoreduction arises from their general lack of photostability, which may lead to the formation of polymer photodegradation products, and therefore to the overestimation of the product yields.[7] For that reason, only photostable polymers are suitable for this application. In this context, one of the open questions is how far we can tune CPPs to drive highly demanding photocatalytic reactions such as CO_2 photoreduction. To shed some light on this point, this work reports the use of hybrids containing photostable boron-centered fluorophores as photocatalysts for UV/visible light driven solar fuels production. To the best of our knowledge, this is the first study reporting the use of CPPs, based on BOPHY and BODIPY dyes, as part of organic–inorganic hybrid materials for gas-phase CO_2 photoreduction. No examples have been found in literature beyond linear conjugated polymers and g-C_3N_4.

2. Results and Discussion

In order to develop our studies, the hybrids CMPBDP@T-10 and IEP-7@T-10 were prepared from TiO_2 (PC500) and the

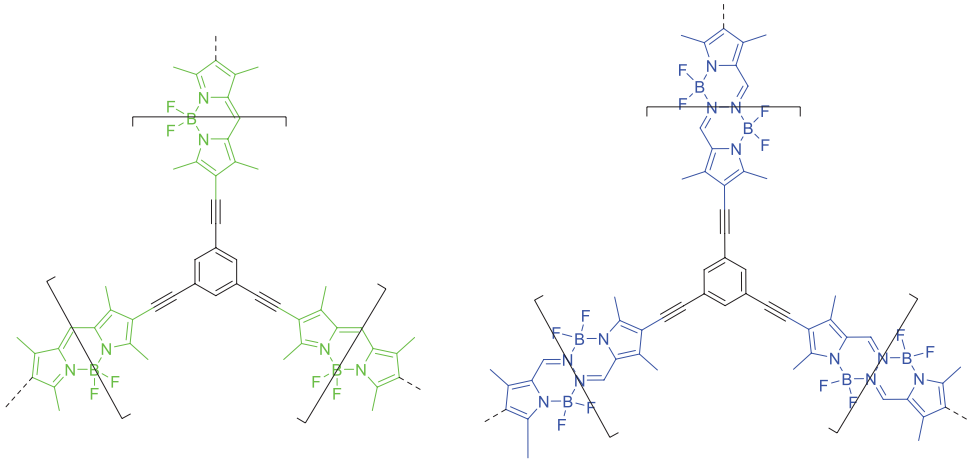

CMPBDP IEP-7

Figure 1. Molecular structure of CPPs based on BODIPY and BOPHY dyes (CMPBDP and IEP-7, respectively). Note that IEP stand for IMDEA Energy Polymers.

selected CPPs based on BODIPY and BOPHY cores (10 wt% CPP), respectively (Figure 1). The percentage weight of both CPPs was confirmed by thermogravimetric analyses TGA (see Figure S2, Supporting Information).

The BODIPY-based polymer, CMPBDP, showed a high Brunauer–Emmett–Teller (BET) specific surface area of 278 $m^2\ g^{-1}$ (Figure S3A, Supporting Information) and a pore volume of 0.046 $cm^3\ g^{-1}$; whereas the BOPHY-based polymer, IEP-7, presented a lower surface area of 56 $m^2\ g^{-1}$ (Figure S3B, Supporting Information) and a pore volume of 0.075 $cm^3\ g^{-1}$.[34] It is worth to note that coupling TiO_2 with CPPs led to similar surface areas for both hybrids (111 and 107 $m^2\ g^{-1}$ for CMPBDP@T-10 and IEP-7@T-10, respectively, see Figure S3C,D, Supporting Information). Considering that TiO_2 sample had a BET specific surface area of 166 $m^2\ g^{-1}$ and a pore volume of 0.44 $cm^3\ g^{-1}$,[36] the most presumable explanation for the similar surface areas of the hybrids is a partial covering of the CPP pores by the TiO_2 nanoparticles.

The chemical composition and structure of the CPPs were determined by attenuated total reflection-Fourier-transform infrared (ATR-FTIR), ^{13}C nuclear magnetic resonance (NMR), and X-ray photoelectron spectroscopy (XPS) spectroscopies. ATR-FTIR spectra (Figure S4, Supporting Information) showed the characteristic bands of the BODIPY (≈2194, 1629, and 1200 cm^{-1}) and BOPHY cores (≈2200 and 1595 cm^{-1}), thus confirming the successful synthesis of both CPPs. Solid-state ^{13}C NMR spectra showed broad peaks between 100–155 ppm, associated with the aromatic carbons atoms from the CPPs structure (Figure S5, Supporting Information). The CMPBDP@T-10 polymer exhibited signals in the range of 5–15 ppm, corresponding to carbon atoms of the methyl groups from the BODIPY moiety (Figure S5A, Supporting Information). On the other hand, IEP-7@T-10 polymer showed two peaks at 82 and 92 ppm as a result of the triple bond group, and a narrow peak at 11 ppm related to the aliphatic C from BOPHY moiety (Figure S5B, Supporting Information). Additionally, the surface chemical composition of CMPBDP@T-10 and IEP-7@T-10 was studied by XPS (Figure S6, Supporting Information). The analysis revealed significant negative deviations of the surface concentration of the CPPs as compared with the nominal value (Table S1, Supporting Information). These observations agree well with the predominant morphology of the hybrids, in which amorphous CPPs are surrounded by the TiO_2 nanocrystals (as an example, see the scanning transmission electron microscopy (STEM) images of CMPBDP@T-10 in Figure S7, Supporting Information), therefore exhibiting a lower effective surface exposure. The outer disposition of TiO_2 over the amorphous CPP nanoparticles was unequivocally confirmed by field emission scanning electron microscopy (FESEM) micrographs and X-EDX analyses (**Figure 2**).

Regarding the electronic structure of the hybrids, the relative energy levels of the HOMO and LUMO of the polymers were estimated by the electrochemical determination of their ionization potential (IP) and electron affinity (EA). For the CMPBDP, the HOMO was calculated to be −5.4 eV, and the LUMO was −3.6 eV, according to its oxidation and reduction potentials (0.84 and −1.21 V, respectively) from cyclic voltammetry (CV) measurements (Figure S8A, Supporting Information). These band energy levels resulted in an electrochemical bandgap of 2.0 ± 0.3 eV (Figure S8B, Supporting Information). IEP-7 exhibited a slightly larger bandgap (2.2 ± 0.3 eV), according to its HOMO and LUMO energies (−6.00 and −3.85 eV, respectively).[34] In both cases, these energy levels reached the thermodynamic requirements for driving both the photocatalytic CO_2 reduction and H_2 evolution. However, CMPBDP possesses higher energy values for both the HOMO and the LUMO compared with the polymer IEP-7, which correlates well with the higher driving force for the electron transfer of the BODIPY-based hybrid. Besides, the narrower bandgap of CMPBDP leads to a more red-shifted absorption maximum (λ_{max} = 536 nm[25] *vs* λ_{max} = 450 nm for IEP-7[34]), which in turn results in more absorbed photons in the visible region that clearly benefits the photocatalytic performance.

Next, the photoactivity of CMPBDP@T-10 and IEP-7@T-10 hybrids was investigated in the UV- and visible-light-driven artificial photosynthesis.

2.1. Photocatalytic CO_2 Reduction

The performance of both CPP@TiO_2 hybrids for CO_2 photoreduction was evaluated in a gas-phase reactor using water as electron donor under UV and visible illumination. Neither metal co-catalysts nor organic sacrificial agents were used in this study in order to conduct the process in a more economic and sustainable manner.

For both hybrids, CH_4, CO, and H_2 were found to be the major products under UV illumination (**Figure 3**A). Besides, methyl formate, ethylene, and ethane were also detected in minor amounts (Table S2, Supporting Information). IEP-7@T-10 showed a significant improvement in CO_2 photoreduction performance compared to bare TiO_2, leading to a four and threefold enhancement of H_2 and CH_4 productions (Table S2, Supporting Information). Besides, ethylene and ethane were also formed over the hybrid, whereas negligible amounts were found over TiO_2.

On the other hand, CMPBDP@T-10 also promoted the formation of CH_4, CO, and H_2, together with methyl formate, ethylene, and ethane as minority by-products (Figure 3A). In this case, CH_4 and H_2 productions quadrupled that obtained with TiO_2, and the productions of ethylene and ethane had a seven and tenfold increase, respectively (Table S2, Supporting Information). There was also a clear improvement of the CH_4/CO ratios, which increased from 0.12 in TiO_2 to 0.42 over the hybrid CMPBDP@T-10. Notably, the photoactivity of CMPBDP@T-10 outperformed most of the state-of-the-art organic–inorganic hybrids for gas-phase CO_2 photoreduction, in the absence of any metal co-catalyst or dopant and under UV illumination (Table S3, Supporting Information).

Interestingly, the photocatalytic performance of this BODIPY-based hybrid surpassed that of the BOPHY-based counterpart, especially regarding CH_4 and C_{2+} productions which increased more than 38% and 29%, respectively with CMPBDP@T-10. Moreover, it is worth noting that the production of CH_4 over CMPBDP@T-10 was almost four times higher than the sum of productions of the bare materials (Table S2, Supporting Information). This finding reveals a clear synergetic effect between the CPP and TiO_2 within the heterojunction.

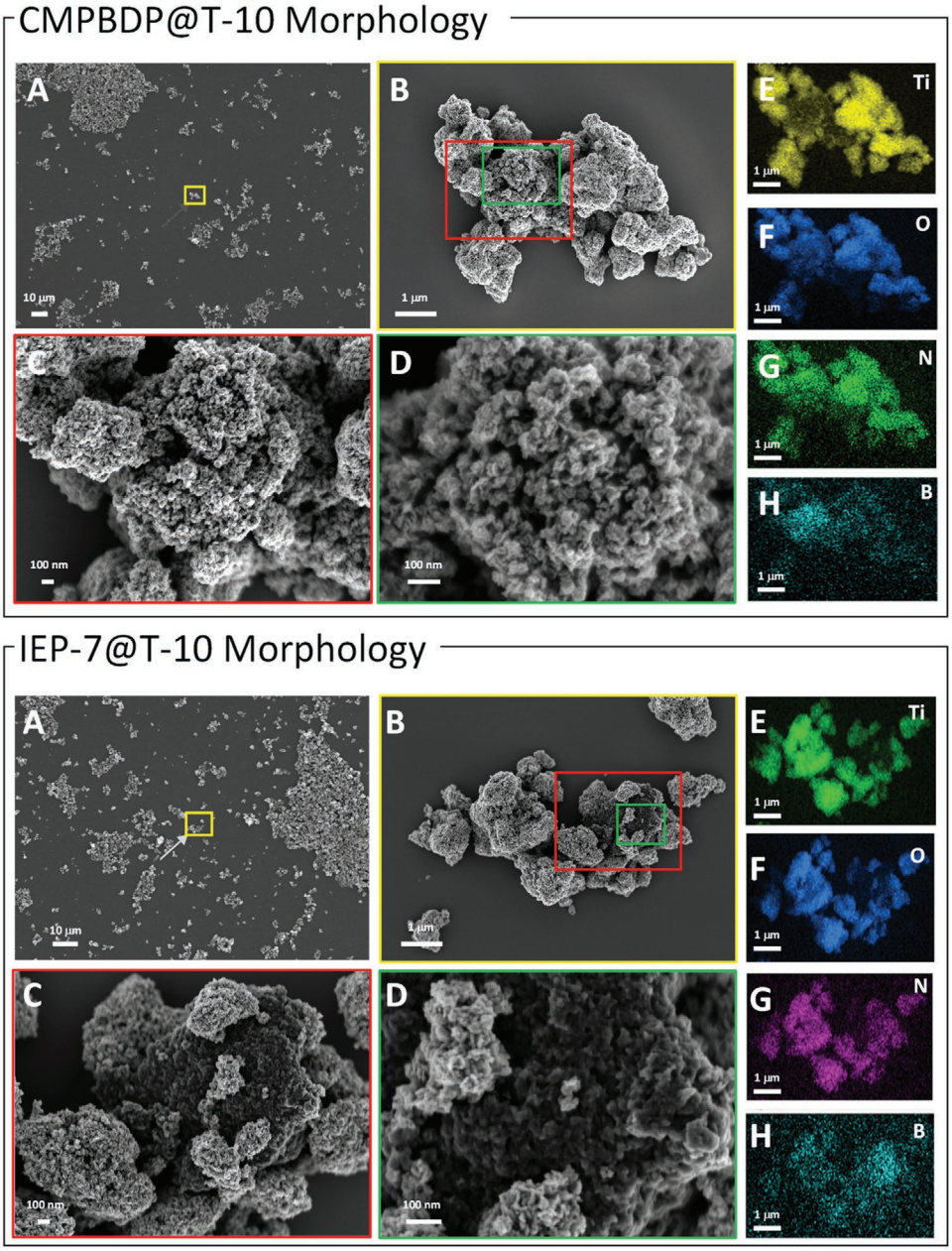

Figure 2. Morphological characterization of CMPBDP@T-10 (top) and IEP-7@T-10 (bottom) hybrids by FESEM. A) Panoramic image. B) Magnification of the squared yellow region in (A). C,D) Magnifications of the red and green rectangles in (B), respectively. E–H) X-EDS microanalysis of titanium, oxygen, nitrogen, and boron, respectively.

A meaningful comparison of the photocatalytic performance consists of the analysis of the electron consumption rate of the photocatalysts,[37,38] by considering the overall number of electrons involved in the formation of each product (i.e., 2, 8, 12, and 14-electron transfer for CO, CH_4/$C_2H_4O_2$, C_2H_4, and C_2H_6, respectively). Figure 3C shows a remarkable higher electron consumption rate of the CMPBDP@T-10 hybrid in comparison to the sole counterparts. Namely, weighted productivities[39] more than doubled that of TiO_2 and even surpassed by 24 times that of the sole polymer (Table S2, Supporting Information), suggesting a higher photocatalytic CO_2 reduction efficiency of the hybrid heterojunction. Further, the photocatalytic performances were also compared in terms of their photonic efficiencies toward CH_4 (Figure 3C). CMPBDP@T-10 hybrid reached 0.13% under UV illumination (λ_{max} = 369 nm), more than tripled that of TiO_2 (≈0.04%).

The photocatalytic activity of CMPBDP@T10 for CO_2 photoreduction was also tested under visible light illumination (400–600 nm). Excitation of the BODIPY dye promoted the generation of e^-/h^+ pairs to drive the reduction of CO_2 mainly toward methyl formate, as well as H_2, CO and small amounts of CH_4 (Figure 3D). As expected, cumulative productions were

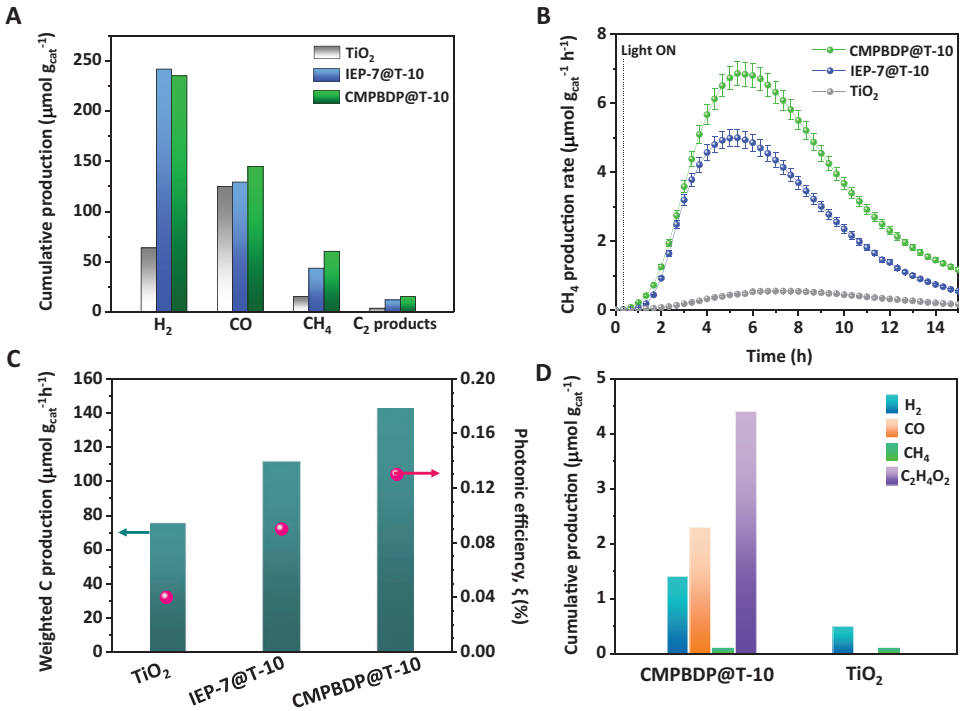

Figure 3. A) Overall cumulative production and B) CH_4 evolution over hybrid heterostructures and TiO_2 in CO_2 photoreduction under 15 h of UV illumination ($\lambda_{max} = 365$ nm) (error bars ±5%). C) Weighted carbon production and photonic efficiency toward CH_4 under UV illumination. D) Cumulative production over CMPBDP@T-10 and TiO_2 under 15 h of visible light illumination (400–600 nm).

significantly lower than under UV illumination, except for methyl formate that almost tripled its value. No methyl formate could be observed over TiO_2, and just small amounts of H_2 and CH_4 were detected.

Next, we conducted a series of control experiments to confirm the photocatalytic nature of the process and to control the carbonaceous contamination on the catalyst's surface. No detectable products were found in the dark or under UV/visible illumination in the absence of catalyst. Further, UV light-driven experiments conducted under CO_2-free atmospheres (i.e., argon, argon + H_2O) led to the formation of certain amounts of H_2, CO, and CH_4 (Figure S9, Supporting Information). We note that, apart from the minimal but unavoidable surface carbon contamination of the semiconductors (<1 wt%), GC analyses detected small amounts of CO_2 (≈less than 200 ppm from air) in the feed composition before starting the illumination. This small carbon contribution, likely coming from impurities of the reagents, may contribute to the formation of carbonate-like species that may act as initiators of reduced C-products.[40] On the basis of our results, the different product distribution obtained under UV and visible-light illumination suggests that a distinct reaction mechanism may take place in the hybrids. According to the literature, the predominant formation of CO and CH_4 under UV illumination from CO_2 photoreduction may proceed via a carbene-like deoxygenation pathway,[41] through surface CO species to CHO/CHOH/CH_3O intermediates to form CH_4, among others. On the other hand, visible light illumination could promote faster hydrogen addition reactions leading to the major formation of CH_3 intermediates and methyl formate.[42]

2.2. Photocatalytic H_2 Production

The photocatalytic activity of both hybrids, CMPBDP@T-10 and IEP-7@T-10, was evaluated in the generation of hydrogen from water using methanol as reductant. In order to explore the synergetic effect between the organic and inorganic semiconductors in the heterostructures, all the photocatalytic experiments were conducted under UV illumination. Note that a series of hybrids composed by several BOPHY-based CPPs were recently deeply studied by our group, being the IEP-7@T-10 the most active.[34]

Figure 4A depicts the cumulative hydrogen production versus time of both hybrids and TiO_2. CMPBDP@T-10 showed the highest hydrogen evolution rate (≈1.2 mmol g_{cat}^{-1} h^{-1}), which was more than 16 and 1.5 times greater than that of TiO_2 and IEP-7@T-10, respectively. Remarkably, the hydrogen evolution rate of CMPBDP@T-10 was 11 times higher than the sum of its components (Figure S10, Supporting Information), evidencing a clear synergy effect between both organic and inorganic semiconductors in the heterostructure. The photonic efficiency with the hybrids surpassed by 4–5 times that of TiO_2, showing values of 0.44% and 0.36% for CMPBDP@T-10 and IEP-7@T-10, respectively.

In the presence of Pt co-catalyst (1 wt% Pt), the H_2 production over CMPBDP@T-10 increased by more than 40-times relative to the hybrid without Pt. Remarkably, this material showed a 6.6-fold higher H_2 production than Pt/TiO_2 (Figure 4B), reaching a photonic efficiency of 20.4%. Notably, this hybrid also increased by more than 1.4-times the state-of-the-art HER reported with organic–inorganic hybrid materials based on TiO_2 (Table S4, Supporting Information).

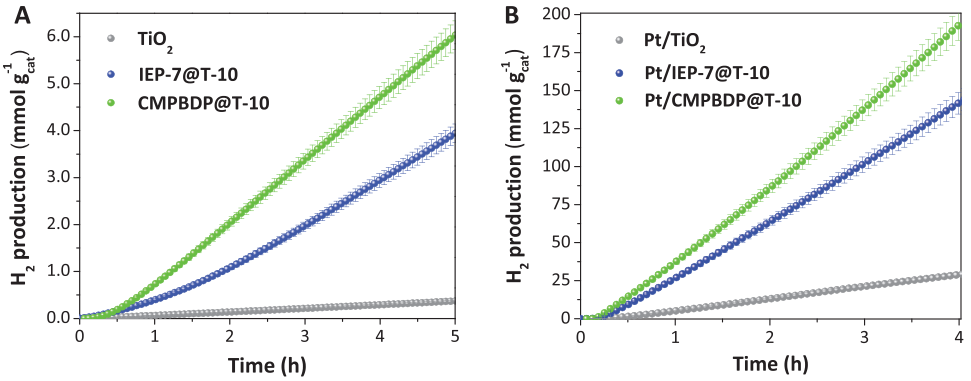

Figure 4. Cumulative hydrogen production versus reaction time of hybrid materials and TiO_2 under UV illumination in the A) absence B) or presence of Pt co-catalyst (1 wt% Pt).

The STEM analysis of CMPBDP@T-10 after reaction showed the preferential photodeposition of Pt nanoparticles (average size of 2.5 nm) on TiO_2 surface (Figure S7C, Supporting Information), rather than on the polymer's surface. Pt nanoparticles were clearly revealed as brilliant points in high-angle annular dark-field (HAADF)–STEM images (Figure S7D, Supporting Information).

One of the major limitations of polymers for photocatalytic applications is their limited photochemical stability. In fact, it is well-known that linear polymers tend to degrade under prolonged illumination.[43] Here, no sign of catalyst deactivation was observed in recycling experiments (Figure S11, Supporting Information) for at least 3 UV-dark cycles, which demonstrates that the complex inter-crossed structure of CMPBDP conferred excellent photostability and reusability to the hybrid CMPBDP@T-10 under our reaction conditions.

Further, the structural photostability of CMPBDP@T-10 was studied before and after the photocatalytic H_2 production tests by FTIR and XPS analyses. ATR-FTIR spectra (Figure S12, Supporting Information) showed that the characteristic C=N stretching (≈1629 cm^{-1}) of CMPBDP was retained after the photocatalytic tests. No further changes were clearly found in the spectrum after reaction, probably due to the predominant overlapping with the TiO_2 features as a result of the low polymer content (10 wt%) in the hybrid. The XPS F 1s spectra showed a maximum at 684.5 eV (Figure S6A, Supporting Information), associated with the BF_2 unit in the BODIPY. The N 1s peak (Figure S6B, Supporting Information), centered at around 400.5 eV, is within the binding range of N 1s for organic materials.[44] However, the N 1s peak position is slightly higher than those reported for pyridinic (around 398.6 eV) and pyrrolic (around 400.0 eV) compounds.[45] The higher binding energy may be result from a strong interaction with the BF_2 center, whose coordination results in a positive charge shared between the two N atoms in the dipyrromethene. Both N 1s and F 1s spectral features remained unaltered after running the photocatalytic tests (Figure S6, Supporting Information), which suggests that the polymer remains stable under the reaction conditions. Consistently, the F/Ti ratio of the hybrid´s surface, before and after the photocatalytic test, showed that the composition remained constant within the experimental error (≈F:Ti = 2:100). These findings demonstrate the excellent photostability of CMPBDP@T-10 under the tested reaction conditions.

2.3. Charge Dynamics Studies

Further, to deeply understand the electron transfer mechanism governing the photocatalytic activity of the hybrids, we developed spectroscopic studies from the ns to μs timescale, using steady-state photoluminescence (PL), time-resolved PL, and transient absorption spectroscopy (TAS). In a recent work,[34] we reported a Type II heterojunction mechanism between the BOPHY-based IEP-7 and TiO_2. Now, we put our focus on CMPBDP@T-10 to study the charge transfer mechanism and to ascertain the role of transient species in its photocatalytic activity.

First, steady-state and time-resolved photoluminescence emissions of CMPBDP@T-10 and IEP-7@T-10 hybrids were evaluated in solid-state, and compared with that of bare TiO_2 (**Figure 5**A). The analysis of both hybrids under steady-state conditions revealed a clear quenching of TiO_2 fluorescence due to the presence of the polymers. However, this behavior was associated with a filter effect instead of a real quenching, since the fluorescence lifetimes (τ_F) showed an opposite behavior, even resulting in a slight increase in τ_F for hybrids than for bare TiO_2 (Figure 5A inset). The decay trace fit resulted in a narrow but reproducible difference, namely τ_F = 3.40 ns for TiO_2 and τ_F = 3.46 and 3.48 ns for CMPBDP@T-10 and IEP-7@T-10, respectively (Figure S13, Supporting Information). This small difference in τ_F has been also observed in composites based on SrO as IS and carbon nitride as OP (SrO-clusters@amorphous g-C_3N_4).[46] These results suggest an interfacial charge transfer from the LUMO of the polymer to the conduction band (CB) of TiO_2, which should mostly occur in a timescale greater than a few nanoseconds.

To demonstrate our hypothesis, hybrids and bare TiO_2 were studied using TAS. After excitation (λ_{exc} = 355 nm), the transient absorption (TA) spectrum of TiO_2 showed a continuous absorption in all spectrum window, exhibiting a small band at ≈455 nm (Figure S14A, Supporting Information) which is usually assigned to trapped holes,[47–51] although other works reported the TA of trapped electrons between 400 and 650 nm by nanosecond TAS.[49–53]

Here, the identification of the transients (electrons or holes) was investigated by TAS using exogenous scavengers. First, in aqueous 10% (v/v) methanol solution the temporal profile of TiO_2 at λ_{obs} = 460 nm (Figure S15A, Supporting Information) showed two main contributions; the first one ($\tau \approx$ 51 ns) fitted well to first-order kinetics over the early nanoseconds after the

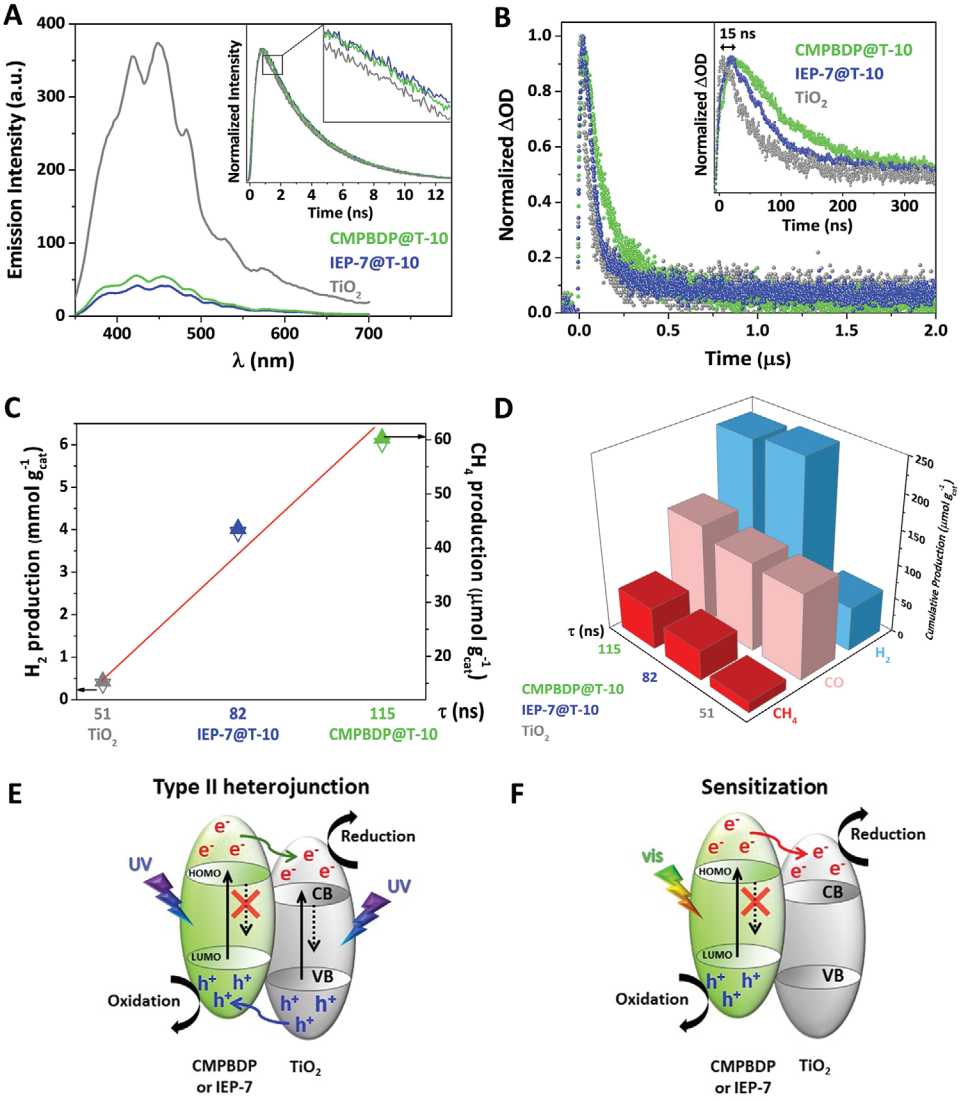

Figure 5. A) Solid-state photoluminescence spectra of TiO_2 (grey) and hybrids heterojunctions (IEP-7@T-10 in blue and CMPBDP@T-10 in green). Inset: Fluorescence decay traces and the corresponding magnification from 1 to 2 ns. B) Transient decay lifetimes (λ_{exc} = 355 nm, λ_{obs} = 460 nm) for TiO_2 (grey), CMPBDP@T-10 (green) and IEP-7@T-10 (blue) in deaerated 10 vol% aqueous methanol suspensions. Inset: Expanded image for the first nanoseconds window. C) Cumulative H_2 production from water splitting reactions or CO_2 photoreduction toward CH_4 (empty and solid triangles, respectively) *versus* transient lifetime for TiO_2 (grey), IEP-7@T-10 (blue) and CMPBDP@T-10 (green). D) Relationship between the evolution of CO_2 photoreduction products and the transient lifetime for TiO_2 (grey), IEP-7@T-10 (blue) and CMPBDP@T-10 (green). E) Type II heterojunction and F) photosensitized charge transfer mechanism of hybrids based on TiO_2 and IEP-7 or CMPBDP.

laser pulse, followed by a longer second contribution in the μs timescale ($\tau \approx 790$ ns). Since methanol is a very efficient hole scavenger,[47] this results suggest that this signal can be attributed to electrons. Indeed, when TAS kinetic was measured in the absence of methanol, a faster decay was detected (Figure S16, Supporting Information).

On the other hand, it is widely known that Pt acts as an electron acceptor over the TiO_2 surface.[54] Thus, in the presence of H_2PtCl_6 (Figure S17, Supporting Information), we observed a complete quenching of the transient spectra and the kinetic trace of TiO_2, associated with the reduction of Pt^{4+} to Pt^0 on the titania surface upon photoexcited electron trapping.[52,54]

The transient absorption of the CMPBDP@T-10 hybrid increased with respect to that of bare TiO_2 (Figure S14B, green trace, Supporting Information), indicating a decrease in the electron–hole recombination in the presence of the polymer. A similar trend was also observed for IEP-7@T-10.[34] Nevertheless, bare polymers did not show any absorption under our measurement conditions, suggesting an intermolecular interaction in the hybrid materials (Figure S14B, Supporting Information). Interestingly, CMPBDP@T-10 showed a remarkable enhancement of the transient lifetime (≈2.3-times greater τ) compared to pristine TiO_2 (Figure 5B and S15B left-side, Supporting Information), which was accompanied by a small but significant delay of 15 ns in the lifetime profile during

the first nanoseconds after the laser pulse (Figure 5B inset). In contrast, no further changes were observed for the longer second contribution (Figure S15B right-side, Supporting Information), similarly to IEP-7@T-10 hybrid[34] (Figure S15C, Supporting Information), and previous observations over truxene-based CPPs.[57] This assertion was even more evident after fitting the monitored lifetimes to a bi-exponential function (Figure S15, right-side, Supporting Information). The decays of the hybrids experienced a huge increase in τ_{TiO_2} in the first shortest contribution (τ = 50, 82, and 115 ns for TiO_2, IEP-7@T-10, and CMPBDP@T-10, respectively), while the second longest τ in the microsecond scale remained unaltered (less than 5% error). These fits also revealed that the shortest contribution practically comprised the entire population of the excited electrons, according to the obtained pre-exponential values (denoted by A symbol in Figure S15 A–C, right-side, Supporting Information).

For the CMPBDP@T-10 hybrid, the increase of the first component at the observation wavelength (λ_{obs} = 460 nm) clearly indicates the influence that CPP exerts on the TiO_2 signal, and corroborates the clear and unequivocal fast electron transfer that takes place from the LUMO of CMPBDP to the CB of TiO_2 after bandgap excitation. This charge transfer predominantly takes place through a Type II mechanism (Figure 5E), in which half-redox reductions occur on the CB of TiO_2 while the oxidation takes place in the ground state of the polymer surface. This finding correlates well with the preferential photodeposition of Pt nanoparticles on TiO_2 surface, as confirmed by HAADF-STEM images (Figure S7D, Supporting Information). Both observations further support a predominant Type II heterojunction for CMPBDP@T-10, where reduction takes place on the surface of TiO_2.

Additional TAS experiments in the presence of H_2PtCl_6 revealed a complete quenching of the TA spectra of the hybrids (Figure S17A, Supporting Information). This finding is indicative of the presence of Pt over the reductive counterpart of the hybrid material.

On the other hand, a direct relationship was found between the transients of the hybrids and their photocatalytic activity toward hydrogen production and CO_2 photoreduction. For both hybrids, the increase in τ explains the higher photocatalytic activity toward H_2 evolution (Figure 5C left-side) and CO_2 reduction (Figure 5C right-side and 5D). Interestingly, plotting lifetimes against photoactivity (Figure 5C) revealed a direct correlation between the transients and the corresponding hydrogen production and CO_2 conversion to CH_4. The transient signal of CMPBDP@T-10 hybrid was 2.3 times higher than TiO_2, supporting the synergetic effect between the CPP and the inorganic semiconductor via a type II heterojunction charge transfer mechanism (Figure 5E, left-side). The distinct photocatalytic response of both hybrids could be explained by their differences in their molecular and electronic structures (Figure 1 and Figure S8, Supporting Information).

To provide spectroscopic evidence supporting the electron transfer from CMPBDP to TiO_2 in the hybrids under visible illumination, time-resolved photoluminescence and transient absorption experiments were performed at λ_{exc} = 445 nm (at which only the polymer absorbs). **Figure 6**A shows the time-resolved photoluminescence measurements of CMPBDP and CMPBDP@T-10 using a cut-off filter at 550 nm, where only the polymer exhibits photoluminescence (Figure S18, Supporting Information). The decay of CMPBDP resulted in a lifetime of τ = 320 ps (Figure 6A, magenta open circles). As a control, no signal was observed through a 450 nm filter since the polymer does not emit in this wavelength (Figure 6B, magenta solid circles, and Figure S18, Supporting Information). Likewise, as expected, no signal was detected for bare TiO_2 at λ_{exc} = 445 nm (Figure 6A right, grey open triangles) in both spectral windows (cut-off filters at 450 or 550 nm). In the case of the hybrid heterostructure, coupling CMPBDP and TiO_2 led to a clear decrease in the photoluminescence lifetime (τ = 282 ps, λ_{obs} = 550 nm) (Figure 6A, green open circles). Besides, an additional signal appeared in a 450 nm window (τ = 255 ps), which can be only associated with the TiO_2 emission (Figure 6B, green open triangles). These findings provide unequivocal proof of an electron transfer from the conduction band of the CMPBDP to titania, following a photosensitized mechanism (see Figure 5F).

As a further piece of evidence, TAS experiments at λ_{exc} = 450 nm were performed using 10% v/v aqueous methanol solutions to simulate the reaction media employed in H_2 evolution studies. Control measurements with TiO_2 did not show any signal under 450 nm of laser pulse excitation (Figure 6C, grey). However, TAS measurements of CMPBDP@T-10 showed the appearance of a broad signal in the entire spectral window, which was attributed to the electrons transferred to TiO_2 (Figure 6C, green). The kinetic trace monitored at 460 nm showed an increase in the signal after 20 ns of laser pulse excitation (Figure 6D), in good agreement with an electron transfer from the polymer to TiO_2 following a photosensitized mechanism.[55,56] The expected decrease in the signal of CMPBDP in the hybrid was not observed due to the overlap with the TiO_2 fingerprint.

3. Conclusions

This work presents the use of hybrid heterostructures based on CPPs as efficient photocatalysts for CO_2 photoreduction and H_2 evolution. Coupling TiO_2 with BOPHY and BODIPY based CPPs led to the creation of a Type II heterojunction with more efficient charge separation and transfer than the sole counterparts. Both hybrids were active in the photocatalytic conversion of CO_2 and water under mild conditions, in the absence of any metal co-catalyst or dopant. CMPBDP@T10 reached a photonic efficiency of 0.11% toward CH_4 (under UV illumination, λ_{max} = 365 nm), more than tripling that of TiO_2 (≈0.03%). The same hybrid, CMPBDP@T10, reached a hydrogen production of ≈6 mmol g^{-1} under UV illumination for 5 h, surpassing by 16-times the benchmark TiO_2. Photodeposition of 1 wt% Pt dramatically increased the hydrogen production to 200 mmol g_{cat}^{-1} after 4 h, reaching a photonic efficiency of 20.4% and increasing by more than 1.4-times the state-of-the-art reported productions with organic–inorganic hybrid materials based on TiO_2. The superior activity of the BODIPY-based hybrid is ascribed to the higher reduction potential of CMPBDP over the BOPHY-based IEP-7, and on the other hand, to the more efficient electron–hole separation in the BODIPY dye. These findings result in a higher driving force for the electron transfer and a longer

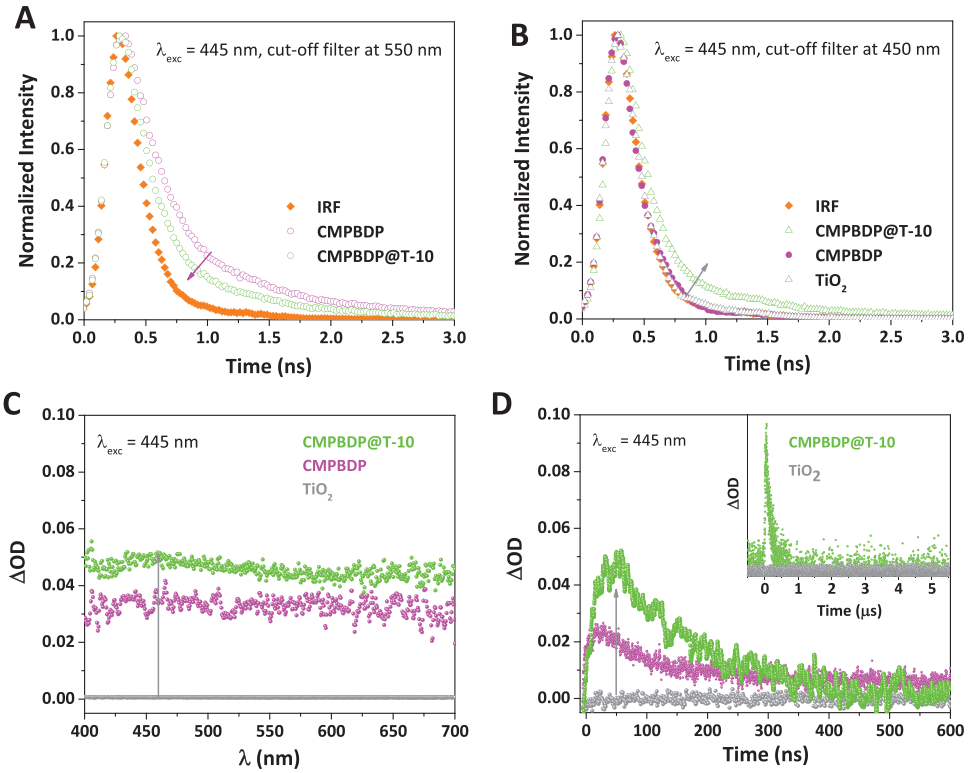

Figure 6. Photoluminescence time-resolved traces recorded at λ_{exc} = 445 nm using a cut-off filter at A) 550 nm or B) 450 nm for TiO_2 (grey) and CMPDBP (magenta) and its corresponding hybrid CMPBDP@T-10 (green) in solid state. The instrumental response function (IRF, orange) is included as reference. Transient absorption spectra (λ_{exc} = 445 nm, C) or decay traces (λ_{exc} = 445 nm, λ_{obs} = 460 nm, D) recorded for TiO_2 contribution in absence (grey) or presence (green) of CMPBDP in the hybrid CMPBDP@T-10 in deaerated 10 vol% aqueous methanol suspensions. The corresponding absorption spectrum and kinetics for CMPBDP (magenta) is included for comparison.

carriers' lifetime, which directly lead to an enhanced performance of the CMPBDP@T-10 hybrid. These results highlight the great potential of highly tunable and photostable CPPs for solar fuels production, as well as for a multitude of light-mediated energy applications.

4. Experimental Section

Materials Preparation: Two CPPs based on BODIPY (CMPBDP[25]) and BOPHY (IEP-7,[33] IEP stands for IMDEA Energy Polymer) cores were synthesized by a palladium-catalyzed Sonogashira–Hagihara cross-coupling reaction from 1,3,5-triethynilbencene, as common core moiety, and their corresponding diiodo-substituted BODIPY and BOPHY monomers, respectively (see chemical structures in Figure 1). Further details of the synthesis procedure of CPPs can be found in previous publications.[25,33]

To perform the studies, hybrid materials composed of 10 wt% of the selected CPP and TiO_2 were prepared, which were labeled as CMPBDP@T-10 and IEP-7@T-10. This composition was selected on the basis of the experience with other CPPs@TiO_2 hybrid series.[34,57] As a general procedure for the hybrids, firstly, TiO_2 anatase (PC500 from CrystalACTIV) was calcined at 400 °C for 4 h in order to remove all the possible organic impurities. Both TiO_2 and the corresponding synthesized CPP (i.e., CMPBDP or IEP-7), at 10 wt% CPP loading with respect to the total amount of catalyst, were dispersed in a mixture of water/acetonitrile (1:1 v/v) and sonicated for 15 min. Afterward, the solvents were removed using a rotary evaporator at 50 °C. The resulting products were ground into powder and dried in the oven at 100 °C under vacuum.

Materials Characterization: Thermogravimetric analyses and differential thermal analyses (TGA/DTA) were recorded in air stream on a thermobalance TGA-DSC water vapor furnace (STA 449 F3 Netzsch). The samples were heated from 30 to 1000 °C with a heating rate of 5 °C min^{-1}.

N_2 physisorption: Nitrogen adsorption and desorption isotherms were measured at 77 K, using an AUTOSORB instrument from Quantachrome. Prior to measurements, the samples were degassed for 12 h at 100 °C. The specific surface area was determined by the BET method, while the total pore volume was calculated using the t-plot method.

ATR-FTIR: ATR-FTIR spectra were collected in a Thermo Fisher Scientific Nicolet 6700 equipped with a ceramic source, KBr beam splitter and a DTGS detector. The spectra were collected in the range 4000–400 cm^{-1} using 64 co-added scans and powdered samples.

^{13}C solid-state NMR: NMR spectra were recorded with a Bruker AVIII/HD spectrometer (Larmor frequency of 100 MHz for ^{13}C) using a 2.5 and 4 mm magic angle spinning (MAS) probes spinning at a rate of 12 and 8 kHz for ^{13}C solid-state MAS NMR measurements. The ^{13}C CP-MAS spectra were obtained using a contact time of 3.0 ms and a relaxation time of 5 s. The number of scans used for the ^{13}C CP-MAS spectra was chosen such that the S/N is greater than or equal to 20.

FESEM: FESEM images were taken with an FESEM JEOL JSM-7900F equipment provided with an energy-dispersive X-ray spectroscopy detector (X-EDS) Ultim Max 170 Oxford Instruments model. The images have been processed by means of Aztec de Oxford instruments software.

STEM: STEM images of the Pt/CMPBDP@T-10 hybrid were acquired on a TEM JEOL 2100 instrument at an accelerating voltage of

200 KV. Elemental detection was carried out with an energy dispersive spectroscope (EDS) microanalysis system.

XPS: XPS was performed with a lab-based spectrometer (SPECS GmbH, Berlin) using monochromated Al Kα source ($h\nu$ = 1486.6 eV) operated at 50 W as excitation source. In the spectrometer, the X-ray was focused with a µ-FOCUS 600 monochromator onto a 300 µm spot on the sample, and the data were recorded with a PHOIBOS 150 NAP 1D-DLD analyzer in a fixed analyzer transmission (FAT) mode. The pass energy was set to 40 eV for survey scans and 20 eV for high-resolution regions. The binding energy scale was calibrated using Au $4f_{7/2}$ (84.01 eV) and Ag $3d_{5/2}$ (368.20 eV). Recorded spectra were additionally calibrated against the C 1s internal reference. Data interpretation was done with Casa XPS. Shirley or two-point linear background was used depending on the spectrum shape. Surface chemical analysis was done based on the peak area of high-resolution spectra and the CasaXPS sensitivity factors (where RSF of C 1s = 1.000).

CV: CV measurements were performed in a three-electrode glass cell with a quartz window containing 0.1 M of tetra-*n*-butylammonium hexafluorophosphate $[(^{n}Bu)_4)N]PF_6$ in acetonitrile as the electrolyte. A paste containing the CPP was prepared by mixing 5 mg of the polymer, 45 µL of Nafion perflorinated resin solution, and 450 μL of isopropanol. The paste was deposited and dried on the platinum working electrode. The counter electrode was a platinum wire, and an Ag wire electrode was used as a pseudo-reference (calibrated with ferrocene). Voltage and current density were measured with a potentiostat-galvanostat PGSTAT204 provided with an integrated impedance module FRAII (10 mV of modulation amplitude at 400 Hz). Current and voltage signals were measured through an Autolab PGSTAT204 potentiostat/galvanostat station. The curves were calibrated with the ferrocene/ferrocenium (Fc/Fc^+) pair. The HOMO and LUMO energy levels of the CPP were obtained according to the Equations (1) and (2)

$$E_{HOMO}\,(eV) = -\left[5.2 - E_{1/2}\left(Fc/Fc^+\right) + E_{ox,onset}\right] \quad (1)$$

$$E_{LUMO}\,(eV) = -\left[5.2 - E_{1/2}\left(Fc/Fc^+\right) + E_{red,onset}\right] \quad (2)$$

The half-wave potential of the Fc/Fc^+ redox couple was estimated from Equation (3)

$$E_{1/2}\left(Fc/Fc^+\right) = \left(E_{ap} + E_{cp}\right)/2 \quad (3)$$

E_{ap} and E_{cp} are the anodic and cathodic peak potentials, respectively.

Steady-state and time-resolved photoluminescence: Fluorescence experiments for solid powdered samples were carried out with a fluorescence spectrometer Perkin Elmer LS 55, with an excitation wavelength of 300 nm and using a cut-off filter at 350 nm in front-face mode. Time resolved florescence measurements were recorded in a Mini Tau system provided with a band pass filter, using an EPL-375 ps pulsed diode laser with emission at 372 or 445 nm as excitation source (both from Edinburgh Instruments). The instrument response function (IRF) signal was included as reference.

TAS: Laser flash photolysis measurements were carried out with a LP980 equipment from Edinburgh Instruments (LP980), based on an optical parametric oscillator (OPO) pumped by the third harmonic of a Nd:YAG laser (EKSPLA). The selected excitation wavelength for the measurements was 355 or 445 nm with single low energy pulses of 1 mJ per pulse of ≈5 ns duration, while a pulsed xenon flash lamp (150 W) was employed as detecting light source. The probe light is dispersed through a monochromator (TMS302-A, grating 150 lines mm^{-1}) after it has passed the sample and then reaches a PMT detector (Hamamatsu Photonics) to obtain the temporal profile. The absorbance of all samples was kept at ≈0.3 at λ_{exc} = 355 or 455 nm as dispersed solutions. All transient spectra were recorded at room temperature using 10 × 10 mm^2 quartz cells, which were bubbled for 15 min with N_2 before acquisition. TAS experiments (ns–μs timescale) were performed to investigate the generation, recombination, and dynamic charge transfer events in the hybrids and the corresponding bare materials upon photon absorption. Measurements were conducted using 10 vol% aqueous methanol suspensions to simulate the reaction media in photocatalytic H_2 evolution studies. Since one cannot reproduce the conditions employed for the gas-phase CO_2 photoreduction experiments in the laser flash photolysis system, the optoelectronic properties of the catalysts were measured in aqueous conditions and correlated with their activity toward CO_2 photoreduction.

Photocatalytic Activity Evaluation: CO_2 photoreduction: Photocatalytic experiments were conducted in continuous-flow mode in a home-made reaction system. The powdered catalyst (0.1 g) was deposited on a glass microfiber filter. UV illumination was carried out using four 6 W lamps with a maximum wavelength at 369 nm and an average intensity of 47.23 W m^{-2} (measured by a Blue-Wave spectrometer in the range 330–400 nm, see Figure S1A, Supporting Information). A 30 W white light-emitting diode (LED) was used for visible-light illumination (average intensity 53.89 W m^{-2} measured in the region 400–600 nm, see Figure S1B, Supporting Information). Compressed CO_2 (≥99.9999%, Praxair) and water (Milli-Q), were passed through a controlled evaporation mixing unit, maintaining a molar ratio of 7.25 (CO_2:H_2O). The reaction conditions were set at 2 bar and T = 50 °C. In-line gas chromatography (Agilent 7890A) analyses were performed to detect the reaction products. The GC was equipped with two separation branches, one equipped with two semicapillary columns (BR-Q Plot and BR-Molesieve 5A) and one with thermal conductivity detector, a flame ionization detector (FID), and a methanizer. The second separation branch consisted of a capillary column (CP-Sil 5B) and a second FID. Before starting the experiments, the reactor was first degassed under vacuum and then purged for 1 h using argon (100 mL min^{-1}) to remove any residual organic compounds weakly adsorbed to the surface of the catalyst. Then, the reactor was flushed with the CO_2 and water mixture for 1 h to establish an adsorption–desorption balance at the reaction temperature. Analogously, control tests under argon and humid argon atmospheres were performed following the same reaction procedure but changing the feeding flow. All photocatalytic tests were investigated over a period of 0–15 h of irradiation time and repeated at least twice to assure a relative error within ±5%.

The electron consumption rate of the photocatalysts in the CO_2 photoreduction process was calculated using the following equation

$$R_{electron} = 2{\cdot}r(CO) + 8{\cdot}r(CH_4) + 8{\cdot}r(C_2H_4O_2) + 12{\cdot}r(C_2H_4) + 14{\cdot}r(C_2H_6) \quad (4)$$

where $R_{electron}$ is the rate of electron consumption, numbers represent the electrons involved in the formation of each product (x), and $r(x)$ are the corresponding product rates (µmol g_{cat}^{-1} h^{-1}).

Hydrogen production: Photocatalytic experiments were conducted in a Pyrex glass double-walled reactor, which consisted of a three-mouth cylindrical flask with an effective volume of 130 mL. For the experiments, 0.025 g of photocatalyst was added to a 10 vol% methanol aqueous solution. The reactor was tightly closed and maintained at atmospheric pressure and at 20 °C by recirculating water from a cooling system. Argon was flowed through the suspension at 60 mL min^{-1} to purge the system and to act as carrier gas. The suspension was magnetically stirred in the dark until air was removed (verified by GC) and then irradiated by a 150 W medium-pressure Hg immersion lamp (Figure S1C, Supporting Information). H_2 evolution was monitored every ≈3 min by means of an Agilent 490 micro-GC equipped with a molecular sieve column and a TCD detector. For the reactions using Pt as co-catalyst, the metal was photodeposited in situ on the catalyst surface by dissolving the appropriate amount of $H_2PtCl_6 \cdot H_2O$ to obtain 1 wt% Pt nominal loading.

Photonic efficiency (ζ): Photonic efficiencies were calculated as the ratio between the rate of reaction and the incident photon flux, according to Equation (5)[58]

$$\zeta = \frac{dN/dt}{\int_{\lambda_1}^{\lambda_2} q^0_{p,\lambda}\, dt} \quad (4)$$

where dN/dt represents the production rate (CH_4 or H_2 in the case of CO_2 photoreduction or H_2 production experiments, respectively), and $q^0_{p,\lambda}$ is the incident spectral photon flux within a defined wavelength

range (e.g., 250–400 or 400–600 nm for UV and visible light-driven experiments). The incident spectral photon flux was calculated from the lamps emission spectra (see Figure S1, Supporting Information), recorded with a StellarNet UVNb-50 radiometer connected to an optical fiber. The superscript 0 (zero) emphasizes that the incident number of photons (prior to absorption) is also considered.

Supporting Information

Supporting Information is available from the Wiley Online Library or from the author.

Acknowledgements

This work received funding from the European Union's Horizon 2020 research and innovation program under European Research Council (ERC) through the HyMAP project (grant agreement No. 648319) as well as the Marie Skłodowska-Curie grant agreement No 754382. Financial support was received from AEI-MICINN/FEDER, UE through the Nympha Project (PID2019-106315RB-I00), the regional government of "Comunidad de Madrid" and the European Structural Funds through their financial support to FotoArt-CM project (S2018/NMT-4367). Besides, Fundación Ramon Areces funded this work through the ArtLeaf project. L.C. acknowledges the European Union's Horizon 2020 research and innovation program under the Marie Skłodowska-Curie grant agreement No 754382, Got Energy Talent. M.L. and T.N. extend thanks to AEI-MINECO/MICINN and European Social Fund for Ramón y Cajal (RyC-2015-18677), and Juan de la Cierva Formación (FJC2019-040159) grants, respectively.

Conflict of Interest

The authors declare no conflict of interest.

Author Contributions

L.C., M.L., J.M. and V.A.P.O. conceived the idea. T.N. and C.G. L.-C. synthesized the CPPs and the hybrids. L.C. performed the CO_2 photoreduction tests. L.C. and T.N. carried out and analyzed the photocatalytic H_2 evolution tests. L.C. and T.N. characterized the hybrids. M.G.-M. performed the charge dynamics studies. F.O. acquired the XPS spectra. L.C. prepared and edited the manuscript. All authors contributed to the discussion of the results and the revision of the manuscript.

Data Availability Statement

The data that supports the findings of this study are available in the supplementary material of this article.

Keywords

artificial photosynthesis, charge dynamics, conjugated porous polymers, hybrid heterostructures, solar fuels, transient absorption spectroscopy

Received: June 4, 2021
Revised: July 8, 2021
Published online:

[1] J. Su, L. Vayssieres, *ACS Energy Lett.* **2016**, *1*, 121.
[2] M. E. El-Khouly, E. El-Mohsnawy, S. Fukuzumi, *J. Photochem. Photobiol., C* **2017**, *31*, 36.
[3] J. Yang, Y. Guo, W. Lu, R. Jiang, J. Wang, *Adv. Mater.* **2018**, *30*, 1802227.
[4] H. J. Sayre, L. Tian, M. Son, S. M. Hart, X. Liu, D. M. Arias-Rotondo, B. P. Rand, G. S. Schlau-Cohen, G. D. Scholes, *Energy Environ. Sci.* **2021**, *14*, 1402.
[5] S. Chabi, K. M. Papadantonakis, N. S. Lewis, M. S. Freund, *Energy Environ. Sci.* **2017**, *10*, 1320.
[6] C. Bozal-Ginesta, J. R. Durrant, *Faraday Discuss.* **2019**, *215*, 439.
[7] M. Liras, M. Barawi, V. A. de la Peña O'Shea, *Chem. Soc. Rev.* **2019**, *48*, 5454.
[8] T. Zhang, G. Xing, W. Chen, L. Chen, *Mater. Chem. Front.* **2020**, *4*, 332.
[9] R. R. Haikal, A. B. Soliman, M. Amin, S. G. Karakalos, Y. S. Hassan, A. M. Elmansi, I. H. Hafez, M. R. Berber, A. Hassanien, M. H. Alkordi, *Appl. Catal., B* **2017**, *207*, 347.
[10] J. Byun, K. A. I. Zhang, *Mater. Horiz.* **2020**, *7*, 15.
[11] C. Dai, B. Liu, *Energy Environ. Sci.* **2020**, *13*, 24.
[12] D. Taylor, S. J. Dalgarno, Z. Xu, F. Vilela, *Chem. Soc. Rev.* **2020**, *49*, 3981.
[13] V. S. Vyas, V. W. H. Lau, B. V. Lotsch, *Chem. Mater.* **2016**, *28*, 5191.
[14] M. Barawi, L. Collado, M. Gomez-Mendoza, F. E. Oropeza, M. Liras, V. A. de la Peña O'She, *Adv. Energy Mater.* **2021**, 2101530, https://doi.org/10.1002/aenm.202101530.
[15] J. Park, *J. Ind. Eng. Chem.* **2017**, *51*, 27.
[16] C. Xu, W. Zhang, J. Tang, C. Pan, G. Yu, *Front. Chem.* **2018**, *6*, 592.
[17] A. Kamkaew, S. H. Lim, H. B. Lee, L. V. Kiew, L. Y. Chung, K. Burgess, *Chem. Soc. Rev.* **2013**, *42*, 77.
[18] M. Bejar, M. Liras, L. Francés-Soriano, V. Voliani, V. Herranz-Pérez, M. Duran-Moreno, J. M. Garcia-Verdugo, E. I. Alarcon, J. C. Scaiano, J. Pérez-Prieto, *J. Mater. Chem. B* **2014**, *2*, 4554.
[19] L. Francés-Soriano, M. Liras, A. Kowalczyk, A. Bednarkiewicz, M. González-Béjar, J. Pérez-Prieto, *Nanoscale* **2016**, *8*, 204.
[20] J. J. Chen, S. M. Conron, P. Erwin, M. Dimitriou, K. McAlahney, M. E. Thompson, *ACS Appl. Mater. Interfaces* **2015**, *7*, 662.
[21] A. Costela, I. García-Moreno, M. Pintado-Sierra, F. Amat-Guerri, R. Sastre, M. Liras, F. López Arbeloa, J. Bañuelos Prieto, I. López Arbeloa, *J. Phys. Chem. A* **2009**, *113*, 8118.
[22] A. Xie, Z. H. Pan, M. Yu, G. G. Luo, D. Sun, *Chin. Chem. Lett.* **2019**, *30*, 225.
[23] L. Dura, M. Wächtler, S. Kupfer, J. Kübel, J. Ahrens, S. Höfler, M. Bröring, B. Dietzek, T. Beweries, *Inorganics* **2017**, *5*, 21.
[24] B. Zheng, R. P. Sabatini, W. F. Fu, M. S. Eum, W. W. Brennessel, L. Wang, D. W. McCamant, R. Eisenberg, *Proc. Natl. Acad. Sci. USA* **2015**, *112*, E3987.
[25] M. Liras, M. Iglesias, F. Sánchez, *Macromolecules* **2016**, *49*, 1666.
[26] M. Liras, M. Pintado-Sierra, M. Iglesias, F. Sánchez, *J. Mater. Chem. A* **2016**, *4*, 17274.
[27] Y. Lin, J. Yin, X. Li, C. Pan, G. Kuang, *J. Wuhan Univ. Technol., Mater. Sci. Ed.* **2019**, *34*, 440.
[28] T. He, D. Tang, C. Lin, X. Shen, C. Lu, L. Xu, Z. Gu, Z. Xu, H. Qiu, Q. Zhang, S. Yin, *Polymers* **2017**, *9*, 13.
[29] R. París, I. Quijada-Garrido, O. García, M. Liras, *Macromolecules* **2011**, *44*, 80.
[30] G. Li, J. F. Yin, H. Guo, Z. Wang, Y. Zhang, X. Li, J. Wang, Z. Yin, G. C. Kuang, *ACS Omega* **2018**, *3*, 7727.
[31] R. Sola-Llano, J. Jiménez, E. Avellanal-Zaballa, M. Johnson, T. A. Cabreros, F. Moreno, B. L. Maroto, G. Muller, J. Bañuelos, L. Cerdán, I. García-Moreno, S. de la Moya, *Dyes Pigm.* **2019**, *170*, 107662.
[32] I. S. Tamgho, A. Hasheminasab, J. T. Engle, V. N. Nemykin, C. J. Ziegler, *J. Am. Chem. Soc.* **2014**, *136*, 5623.
[33] C. G. López-Calixto, S. Cabrera, R. Pérez-Ruiz, M. Barawi, J. Alemán, V. A. de la Peña O'Shea, M. Liras, *Appl. Catal., B* **2019**, *258*, 117933.

[34] C. G. López-Calixto, M. Barawi, M. Gomez-Mendoza, F. E. Oropeza, F. Fresno, M. Liras, V. A. de la Peña O'Shea, *ACS Catal.* **2020**, *10*, 9804.
[35] C. G. López-Calixto, M. Liras, V. A. De, P. O. Shea, R. Pérez-Ruiz, *Appl. Catal., B* **2018**, *237*, 18.
[36] L. Collado, A. Reynal, F. Fresno, M. Barawi, C. Escudero, V. Perez-dieste, J. M. Coronado, D. P. Serrano, J. R. Durrant, V. A. de la Peña O'Shea, *Nat. Commun.* **2018**, *9*, 4986.
[37] M. Manzanares, C. Fàbrega, J. Oriol Ossó, L. F. Vega, T. Andreu, J. R. Morante, *Appl. Catal., B* **2014**, *150–151*, 57.
[38] X. Li, X. Song, C. Ma, Y. Cheng, D. Shen, S. Zhang, W. Liu, P. Huo, H. Wang, *ACS Appl. Nano Mater.* **2020**.
[39] E. W. Mc Farland, J. Tang, *Mater. Sustainable Energy Appl.* **2010**, *421*, 84.
[40] A. Pougin, M. Dilla, J. Strunk, *Phys. Chem. Chem. Phys.* **2016**, *18*, 10809.
[41] A. Sarkar, E. Gracia-Espino, T. Wågberg, A. Shchukarev, M. Mohl, A. R. Rautio, O. Pitkänen, T. Sharifi, K. Kordas, J. P. Mikkola, *Nano Res.* **2016**, *9*, 1956.
[42] J. Y. Liu, X. Q. Gong, A. N. Alexandrova, *J. Phys. Chem. C* **2019**, *123*, 3505.
[43] E. Pavlidou, K. M. Paraskevopoulos, Z. Terzopoulou, D. N. Bikiaris, *Polym. Degrad. Stab.* **2018**, *153*, 23.
[44] C. D. Wagner, W. M. Riggs, L. E. Davis, J. F. Moulder, *Handbook of X-Ray Photoelectron Spectroscopy*, (Ed: G. E. Muilenberg), Perkin-Elmer, Waltham, MA **1979**.
[45] D. Y. Osadchii, A. I. Olivos-Suarez, A. V. Bavykina, J. Gascon, *Langmuir* **2017**, *33*, 14278.
[46] T. M. Clarke, F. C. Jamieson, J. R. Durrant, *J. Phys. Chem. C* **2009**, *113*, 20934.
[47] J. Tang, J. R. Durrant, D. R. Klug, *J. Am. Chem. Soc.* **2008**, *130*, 13885.
[48] X. Wang, A. Kafizas, X. Li, S. J. A. Moniz, P. J. T. Reardon, J. Tang, I. P. Parkin, J. R. Durrant, *J. Phys. Chem. C* **2015**, *119*, 10439.
[49] R. Qian, H. Zong, J. Schneider, G. Zhou, T. Zhao, Y. Li, J. Yang, D. W. Bahnemann, J. H. Pan, *Catal. Today* **2019**, *335*, 78.
[50] R. Katoh, M. Murai, A. Furube, *Chem. Phys. Lett.* **2010**, *500*, 309.
[51] J. Schneider, M. Matsuoka, M. Takeuchi, J. Zhang, Y. Horiuchi, M. Anpo, D. W. Bahnemann, *Chem. Rev.* **2014**, *114*, 9919.
[52] A. O. T. Patrocinio, J. Schneider, M. D. França, L. M. Santos, B. P. Caixeta, A. E. H. Machado, D. W. Bahnemann, *RSC Adv.* **2015**, *5*, 70536.
[53] T. Yoshihara, R. Katoh, A. Furube, Y. Tamaki, M. Murai, K. Hara, S. Murata, H. Arakawa, M. Tachiya, *J. Phys. Chem. B* **2004**, *108*, 3817.
[54] A. Yamakata, T. Ishibashi, H. Onishi, *J. Phys. Chem. B* **2001**, *105*, 7258.
[55] H. Wang, D. Zhou, Z. Wu, J. Wan, X. Zheng, L. Yu, D. L. Phillips, *Mater. Res. Bull.* **2014**, *57*, 311.
[56] K. Virkki, E. Tervola, M. Ince, T. Torres, N. V. Tkachenko, *R. Soc. Open Sci.* **2018**, *5*, 180323.
[57] A. Valverde-González, C. G. López Calixto, M. Barawi, M. Gomez-Mendoza, V. A. de la Peña O'Shea, M. Liras, B. Gómez-Lor, M. Iglesias, *ACS Appl. Energy Mater.* **2020**, *3*, 4411.
[58] S. E. Braslavsky, A. M. Braun, A. E. Cassano, A. V. Emeline, M. I. Litter, L. Palmisano, V. N. Parmon, N. Serpone, *Pure Appl. Chem.* **2011**, *83*, 931.